On Monotonically Integrated Large Eddy Simulation of Turbulent Flows Based on FCT Algorithms

Fernando F. Grinstein and Christer Fureby

Abstract Non-classical Large Eddy Simulation (LES) approaches based on using the unfiltered flow equations instead of the filtered ones have been the subject of considerable interest during the last decade. In the Monotonically Integrated LES (MILES) approach, flux-limiting schemes are used to emulate the characteristic turbulent flow features in the high-wavenumber end of the inertial subrange region. Mathematical and physical aspects of implicit SGS modeling using non-linear flux-limiters are addressed using the modified LES-equation formalism. FCT based MILES performance is demonstrated in selected case studies including (1) canonical flows (homogeneous isotropic turbulence and turbulent channel flows), (2) complex free and wall-bounded flows (rectangular jets and flow past a prolate spheroid), (3) very-complex flows at the frontiers of current unsteady flow simulation capabilities (submarine hydrodynamics).

1 Background

High Reynolds (*Re*) number turbulent flows are of considerable importance in many fields of engineering, geophysics, and astrophysics. Turbulent flows involve multiscale space/time developing flow physics largely governed by large-scale vortical Coherent Structures (CS's). Typical turbulent energy spectra exhibit a large-wavelength portion dependent on the flow features imposed by geometry and boundary conditions, followed by an intermediate inertial subrange—which becomes longer for higher *Re* and characterizes the virtually inviscid cascade processes, and then by much-faster decaying portion in the dissipation region (e.g., Sect. 5.1.1 below).

F.F. Grinstein (✉)
X-Computational Physics Division, Los Alamos National Laboratory, Los Alamos, NM 87545, USA
e-mail: fgrinstein@lanl.gov

C. Fureby
Dept. of Weapons and Protection, The Swedish Defence Research Agency—FOI, 172 90, Stockholm, Sweden
e-mail: fureby@foi.se

D. Kuzmin et al. (eds.), *Flux-Corrected Transport*, Scientific Computation,
DOI 10.1007/978-94-007-4038-9_3,

Capturing the dynamics of all relevant scales based on the numerical solution of the Navier-Stokes Equations (NSE) constitutes Direct Numerical Simulation (DNS), which is prohibitively expensive for practical flows at moderate-to-high *Re*. On the other end of computer simulation possibilities, the industrial standard is Reynolds-Averaged Navier-Stokes (RANS) modeling, which involves simulating only the mean flow and modeling the effects of the turbulent scales.

Large Eddy Simulation (LES) is an effective intermediate approach between DNS and RANS, capable of simulating flow features which cannot be handled with RANS such as flow unsteadiness and strong vortex-acoustic couplings. Furthermore, LES provides higher accuracy than RANS at reasonable cost but still typically an order of magnitude more expensive. Desirable modeling choices involve selecting an appropriate discretization of the flow problem at hand, such that the LES cutoff lies within the inertial subrange, and ensuring that a smooth transition can be enforced at the cutoff. The main assumptions of LES are that: (i) transport is largely governed by large-scale unsteady features and that such dominant features of the flow can be resolved, (ii) the less-demanding accounting of the small-scale flow features can be undertaken by using suitable Sub Grid Scale (SGS) models.

In the absence of an accepted universal theory of turbulence to solve the problem of SGS modeling, the development and improvement of such models must include the rational use of empirical information. Several strategies to the problem of SGS modeling are being attempted, see e.g., [1], for a recent survey. After more than thirty years of intense research on LES of turbulent flows based on eddy-viscosity models there is now consensus that such approach is subject to fundamental limitations [2]. It has been demonstrated, for a number of flows, that the eigenvectors of the SGS stress and rate-of-strain tensors involved in SGS eddy-viscosity models are not parallel, rendering eddy-viscosity models to be inaccurate.

There have been other proposals that do not employ the assumption of co-linearity of SGS stress and rate-of-strain embedded in the eddy-viscosity models, e.g. the scale-similarity model (SSM) [3] and the Approximate Deconvolution Method (ADM) [4]. Such models may however be numerically unstable, and the more recent efforts have focused on developing mixed models, combining in essence the dissipative eddy-viscosity models with the more accurate but unstable SSM's. The results from such mixed models have been mostly satisfactory but the implementation and computational complexity of these improved combined approaches have limited their popularity. In fact, because of the need to distinctly separate (i.e. resolve) the effects of explicit filtering and SGS reconstruction models from those due to discretization, carrying out such well-resolved LES can typically amount in practice to performing a coarse DNS. As a consequence, it has been argued that the use of hybrid RANS/LES models for realistic whole-domain complex configurations might be unavoidable in the foreseeable future, e.g., [5].

Recognizing the aforementioned difficulties but also motivated by new ideas pioneered at NRL by Boris and collaborators [6, 7], several researchers have abandoned the classical LES formulations and started employing the unfiltered flow equations instead of the filtered ones. Major focus of the new approaches [8, 9] has been on the inviscid inertial-range dynamics and regularization of the under-resolved flow, based

on *ab initio* scale separation with additional assumptions for stabilization, or applying monotonicity via non-linear limiters that implicitly act as a filtering mechanism for the small scales—the original proposal of Boris *et al.* [7]. The latter concept goes back to the 50's to von Neumann and Richtmyer [10], who used artificial dissipation to stabilize finite-difference simulations of flows involving shocks. This artificial dissipation concept also motivated Smagorinsky [11] in developing his scalar viscosity concept based upon the principles of similarity in the inertial range of 3D isotropic turbulence. However, the recognition of the more broadly defined implicit LES (ILES) framework is more recent [12]. In ILES, the effects of the SGS physics on the resolved scales are incorporated through functional reconstruction of the convective fluxes using non-oscillatory—but not necessarily monotonic—finite-volume (NFV) algorithms.

In what follows, we use the modified LES equation formalism to carry out a formal comparative analysis of conventional LES and MILES. The performance of MILES is demonstrated for selected representative case studies including canonical flows, moderately complex free and wall-bounded flows, and extremely complex flows at the frontiers of current flow simulation capabilities. We conclude our presentation by addressing fundamental challenges for further development of the concept of nonlinear Implicit LES (ILES).

2 Conventional LES

For simplicity, we restrict the discussion to incompressible flows described by the Navier-Stokes momentum balance equation,

$$\partial_t(\mathbf{v}) + \nabla\cdot(\mathbf{v}\otimes\mathbf{v}) = -\nabla p + \nabla\cdot\mathbf{S}, \tag{1}$$

in conjunction with the incompressibility (or divergence) constraint $\nabla\cdot\mathbf{v} = 0$, where $\otimes$ denotes the tensorial product, and $\mathbf{S} = 2\nu\mathbf{D}$ and $\mathbf{D} = \frac{1}{2}(\nabla\mathbf{v} + \nabla\mathbf{v}^T)$ are the viscous-stress and strain-rate tensors. The conventional LES procedure [1] involves three basic ingredients:

(i) low-pass filtering by the convolution

$$\bar{f}(\mathbf{x},t) = G * f(\mathbf{x},t) = \int_D G\big(\mathbf{x}-\mathbf{x}',\Delta\big) f\big(\mathbf{x}',t\big)\, d^3\mathbf{x}',$$

with a prescribed kernel $G = G(\mathbf{x},\Delta)$ of width Δ,

(ii) finite volume, element or difference discretization,

(iii) *explicit* SGS modeling to close the low-pass filtered equations.

Applying (i) and (ii), using a second order accurate finite volume algorithm, to (1), and rewriting the results in terms of the *modified equations approach*, i.e., the equation satisfied by the numerical solutions being actually calculated yields [13, 14],

$$\partial_t(\bar{\mathbf{v}}) + \nabla\cdot(\bar{\mathbf{v}}\otimes\bar{\mathbf{v}}) = -\nabla\bar{p} + \nabla\cdot\bar{\mathbf{S}} - \nabla\cdot\mathbf{B} + \mathbf{m}^{\upsilon} + \tau, \tag{2}$$

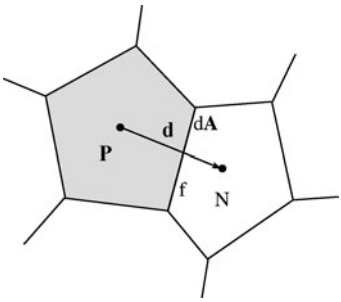

Fig. 1 Grid schematic. P and N denote typical computational cell centers and f an interface; **n** denotes a unit vector normal to the interface, and **A** its area; **d** is the topological vector connecting neighboring cells

where,

$$\mathbf{B} = \overline{\mathbf{v} \otimes \mathbf{v}} - \bar{\mathbf{v}} \otimes \bar{\mathbf{v}}, \qquad \mathbf{m}^v = [G*, \nabla](\mathbf{v} \otimes \mathbf{v} + p\mathbf{I} - \mathbf{S}),$$
$$\tau = \nabla \cdot \left[\left[\frac{1}{6} \nu \nabla^3 \mathbf{v} - \frac{1}{8} \nabla^2 \mathbf{v} \right] (\mathbf{d} \otimes \mathbf{d}) + \cdots \right] \tag{3}$$

are the SGS stress tensor, commutation error term, and the total (convective, temporal and viscous) truncation error, respectively, **I** is the unit tensor, and **d** is the topological vector connecting neighboring control volumes (see Fig. 1), and, $[G*, \nabla] f = \overline{\nabla f} - \nabla \bar{f}$. The commutation error term is often lumped together with the SGS force $\nabla \cdot \mathbf{B}$, prior to modeling, and hence a generalized SGS stress tensor **B** needs to be prescribed in terms of discretized filtered fields for closure of the new equations—which constitutes (iii) above.

Functional modeling consists of the modeling action of the SGS's on the resolved scales. It involves modeling of energetic nature, by which balances of energy are transferred between resolved and subgrid scale ranges, thus accounting for the SGS effects. The energy transfer mechanism from resolved to SGS's is assumed analogous to a Brownian motion superimposed on the large-scale motion. An example of this is the eddy-viscosity approach, in which $\mathbf{B} = -2\nu_k \bar{\mathbf{D}}$ where ν_k is the SGS viscosity—for example, using the Smagorinsky model [11] or the one equation eddy-viscosity model (OEEVM) [15], its principal drawback is the well-established lack of collinearity between **B** and $\bar{\mathbf{D}}$. Natural improvements to these models use anisotropic counterparts based on tensor forms of the SGS turbulent viscosity [16]. These more sophisticated closures involve structural modeling, which attempts to model **B** without incorporating the interactions between SGS and resolved scales. By relying on actual SGS's in the upper resolved subrange—rather than on those modeled through dissipative eddy viscosity—we can better emulate scatter and backscatter, and the modeling procedures won't require assumptions on local isotropy and inertial range. Potential drawbacks arise, however, because structural models are computationally more expensive and typically not dissipative enough; accordingly, mixed models, combined with an eddy-viscosity model, are often used instead.

3 Implicit LES

A key self-consistency issue required in the conventional LES approach involves separating the computing effects of its three basic elements: filtering, discretization, and reconstruction. Filtering and reconstruction contributions must be resolved, i.e., their effective contributions in (2) must be larger than the total truncation error τ. Also, their upper range of represented (but inaccurate) scales interactions must be addressed—in addition to those between resolved and SGS's. Thus, it is useful to examine $\mathbf{B}$ written in the following way,

$$\mathbf{B} = \overline{\mathbf{v} \otimes \mathbf{v}} - \bar{\mathbf{v}} \otimes \bar{\mathbf{v}} = (\overline{\mathbf{v} \otimes \mathbf{v}} - \overline{\mathbf{v}_P \otimes \mathbf{v}_P}) + (\overline{\mathbf{v}_P \otimes \mathbf{v}_P} - \bar{\mathbf{v}} \otimes \bar{\mathbf{v}}) = \mathbf{B}_1 + \mathbf{B}_2, \quad (4)$$

where $\bar{\mathbf{v}}_P$ denotes the (grid) represented velocity scales, $\mathbf{B}_1$ the interaction between represented and nonrepresented scales—which is not known a priori, and therefore must be modeled—whereas $\mathbf{B}_2$ relates to the interaction between filtered and discretized represented scales, and it can be approximated by prescribing an estimated $\mathbf{v}_P$ in the represented-velocity space (i.e., the solution to the so-called *soft deconvolution problem*) [4]. In this framework, a basic structural SGS model, such as the scale-similarity model, provides $\mathbf{B}_2$, and the eventual need of mixed models results from the recognition that $\mathbf{B}_2$ is not dissipative enough so a secondary regularization through $\mathbf{B}_1$ is needed—i.e., an approximation to $\mathbf{v}$ in physical-velocity space must be prescribed (the *hard deconvolution problem*).

Traditional approaches, motivated by physical considerations on the energy transfer mechanism from *resolved* to SGS's, express $\mathbf{B}_1$ with an appropriately functional model (for example, an eddy-viscosity SGS model), and seek sufficiently high-order discretization and grid resolution to ensure that effects due to τ are sufficiently small. However, we could argue that discretization could implicitly provide $\mathbf{B}_1$ if nonlinear stabilization can be achieved algorithmically via a particular class of numerical algorithms or based on regularizing the discretization of the conservation laws. In fact, (2) suggests that most schemes can potentially provide built-in or implicit SGS models enforced by the discretization errors τ, provided that their leading order terms are dissipative. We are thus led to the natural question: To what extent can we avoid the (explicit) filtering and modeling phases of LES (i.e., $\mathbf{B}_2 \equiv \mathbf{0}$ and $\mathbf{m}^v \equiv \mathbf{0}$) and focus on the implicit $\mathbf{B}_1$ provided by a suitably chosen discretization scheme?

Not all implicitly implemented SGS models are expected to work: good or bad SGS physics can be built into the simulation model depending on the choice of numerics and its particular implementation. Moreover, the numerical scheme has to be constructed such that the leading order truncation errors satisfy physically required SGS properties, and hence non-linear discretization procedures will here be required. The analogy to be recalled is that of shock-capturing schemes designed under the requirements of convergence to weak solution while satisfying the entropy condition [17].

4 Monotonically Integrated LES (MILES)

The relevancy of NFV algorithms for ILES of turbulent flows have been motivated [14, 18] by proposing to focus on two distinct inherent physical SGS features to be emulated:

- the anisotropy of high-*Re* turbulent flows in the high-wave-number end of the inertial subrange region, characterized by very thin filaments of intense vorticity and largely irrelevant internal structure, embedded in a background of weak vorticity, e.g., [19],
- the particular (discrete) nature of laboratory observables (only finite fluid portions transported over finite periods of time can be measured) [18].

We thus require that ILES be based on NFV numerics having a *sharp velocity-gradient capturing capability* operating at the smallest resolved scales. By focusing on the inviscid inertial-range dynamics and on adaptive regularization of the under-resolved flow, ILES thus follows very naturally on the historical precedent of using this kind of schemes for shock capturing—in the sense that requiring emulation (near the cutoff) of the high wavenumber-end features of the inertial subrange region of turbulent flows is analogous to spreading the shock width to the point that it can be resolved by the grid.

Although the history of ILES draws on the development of shock-capturing schemes, the MILES concept—as originally introduced by Boris and his colleagues [7] and further developed in our previous work [13, 14]—embodies a computational procedure for solving the NSE as accurately as possible by using a particular class of flux-limiting schemes and their associated built-in (or implicit) SGS models. An intriguing MILES feature is the convection discretization that implicitly generates a nonlinear tensor-valued eddy-viscosity, which acts predominantly to stabilize the flow and suppress unphysical oscillations.

MILES draws on the fact that FV methods filter the NSE over nonoverlapping computational cells Ω_P, with the typical dimension $|\mathbf{d}|$—using a top-hat-shaped kernel, $f_P = \frac{1}{\delta V_P}\int_{\Omega_P} f dV$. In the finite-volume context, discretized equations are obtained from the NSE using Gauss's theorem and by integrating over time with a multistep method parametrized by m, α_i, and β_i,

$$\begin{cases} \dfrac{\beta_i \Delta t}{\delta V_P}\displaystyle\sum_f \left[F_f^{C,\rho}\right]^{n+i} = 0, \\ \displaystyle\sum_{i=0}^{m}\left(\alpha_i(\mathbf{v})_P^{n+i} + \dfrac{\beta_i \Delta t}{\delta V_P}\sum_f \left[F_f^{C,\rho}\mathbf{v}_f + \mathbf{F}_f^{D,v}\right]^{n+i} + \beta_i(\nabla p)_P^{n+i}\Delta t\right) = \mathbf{0}, \end{cases} \tag{5}$$

where α, β and m are parameters of the scheme, and $F_f^{C,\rho} = (\mathbf{v}\cdot d\mathbf{A})_f$ and $\mathbf{F}_f^{C,v} = F_f^{C,\rho}\mathbf{v}_f$ are the convective and $\mathbf{F}_f^{D,v} = (\nu\nabla\mathbf{v})_f d\mathbf{A}$ the viscous fluxes. To complete the discretization, all fluxes at face 'f' need to be reconstructed from the dependent variables at adjacent cells. This requires flux interpolation for the convective fluxes and difference approximations for the inner derivatives in the viscous fluxes.

For conventional LES, it is appropriate to use linear (or cubic) interpolation for the convective fluxes and central difference approximations for the inner gradients in the viscous fluxes. This then results in a cell-centered second- or fourth-order accurate scheme. Scheme stability can be enforced not only by conserving momentum, but also kinetic energy, which ensures robustness without numerical dissipation (which compromises accuracy).

Given (5), the methods available for constructing implicit SGS models by means of the leading order truncation errors are generally restricted to nonlinear high-resolution methods for the convective flux $\mathbf{F}_f^{C,v}$ to maintain second-order accuracy in smooth regions of the flow (such high-resolution methods are at least second-order accurate on smooth solutions while giving well-resolved, non-oscillatory discontinuities) [17]. In addition, these schemes are required to provide a leading order truncation error that vanishes as $\mathbf{d} \to \mathbf{0}$ so that it remains consistent with the NSE and the conventional LES model. We focus here on the certain flux-limiting and correcting methods.

To this end, we introduce a flux-limiter Γ that combines a high-order convective flux-function $\mathbf{v}_f^H$ which is well-behaved in smooth flow regions, with a low-order dispersion-free flux-function $\mathbf{v}_f^L$, being well-behaved near sharp gradients, so that the total flux-function becomes $\mathbf{v}_f = \mathbf{v}_f^H - (1-\Gamma)[\mathbf{v}_f^H - \mathbf{v}_f^L]$. Choosing the particular flux limiting scheme also involves specific selections for $\mathbf{v}_f^L$ and $\mathbf{v}_f^H$. In the analysis that follows, $\mathbf{v}_f^H$ and $\mathbf{v}_f^L$ are assumed to be based on linear interpolation, and upwind-biased piecewise constant approximation, respectively, e.g.,

$$\begin{cases} \mathbf{F}_f^{C,v,H} = F_f^{C,\rho}\left[\ell\mathbf{v}_P + (1-\ell)\mathbf{v}_N - \dfrac{1}{8}(\mathbf{d}\otimes\mathbf{d})\nabla^2\mathbf{v} + O\big(|\mathbf{d}|^3\big)\right], \\ \mathbf{F}_f^{C,v,L} = F_f^{C,\rho}\big[\beta^+\mathbf{v}_P + \beta^-\mathbf{v}_N + \big(\beta^+ - \beta^-\big)(\nabla\mathbf{v})\mathbf{d} + O\big(|\mathbf{d}|^2\big)\big], \end{cases} \tag{6}$$

where $\beta^{\pm} = \frac{1}{2}(\mathbf{v}_f \cdot d\mathbf{A} \pm |\mathbf{v}_f \cdot d\mathbf{A}|)/|\mathbf{v}_f \cdot d\mathbf{A}|$, and $-\frac{1}{8}(\mathbf{d}\otimes\mathbf{d})\nabla^2\mathbf{v}$ and $(\beta^+ - \beta^-)(\nabla\mathbf{v})\mathbf{d}$ are the leading order truncation errors. The flux limiter Γ is to be formulated as to allow as much as possible of the correction $[\mathbf{v}_f^H - \mathbf{v}_f^L]$ to be included without increasing the variation of the solution—e.g., to comply with the physical principles of causality, monotonicity and positivity [7] (when applicable) and thus to preserve the properties of the NSE. To see the effects of this particular convection discretization we consider the modified equations corresponding to the semi-discretized equations (5) with the flux-limiting functions in (6) being used for the convective fluxes,

$$\begin{aligned} \partial_t(\mathbf{v}) + \nabla\cdot(\mathbf{v}\otimes\mathbf{v}) = -\nabla p + \nabla\cdot\mathbf{S} + \nabla\cdot\Bigg[&\mathbf{C}(\nabla\mathbf{v})^T + (\nabla\mathbf{v})\mathbf{C}^T \\ &+ \chi^2(\nabla\mathbf{v})\mathbf{d}\otimes(\nabla\mathbf{v})\mathbf{d} + \left[\frac{1}{6}\nu\nabla^3\mathbf{v} - \frac{1}{8}\nabla^2\mathbf{v}\right](\mathbf{d}\otimes\mathbf{d}) + \cdots\Bigg], \end{aligned} \tag{7}$$

with $\nabla\cdot\mathbf{v} = 0$, and where $\mathbf{C} = \chi(\mathbf{v}\otimes\mathbf{d})$ and $\chi = \frac{1}{2}(1-\Gamma)(\beta^- - \beta^+)$. In particular, we note that in smooth regions, $\Gamma = 1$ implies that $\chi = 0$ and $\mathbf{C} = \mathbf{0}$, and the leading order truncation error becomes $\tau = \nabla\cdot[[\frac{1}{6}\nu\nabla^3\mathbf{v} - \frac{1}{8}\nabla^2\mathbf{v}](\mathbf{d}\otimes\mathbf{d})]$. Comparing

with the analysis of the momentum equation in the framework of the conventional LES approach (equation (2)) suggests that the MILES modified equation incorporates additional dissipative and dispersive terms, and we can consistently identify the implicit SGS stress term,

$$\mathbf{B} = \mathbf{C}(\nabla\mathbf{v})^T + (\nabla\mathbf{v})\mathbf{C}^T + \chi^2(\nabla\mathbf{v})\mathbf{d}\otimes(\nabla\mathbf{v})\mathbf{d}. \tag{8}$$

The implicit SGS stress tensor can according to (8) be decomposed into $\mathbf{B}^{(1)} = \mathbf{C}(\nabla\mathbf{v})^T + (\nabla\mathbf{v})\mathbf{C}^T$ and $\mathbf{B}^{(2)} = \chi^2(\nabla\mathbf{v})\mathbf{d}\otimes(\nabla\mathbf{v})\mathbf{d}$, in which the former is a tensor-valued eddy-viscosity model, while the latter is of a form similar to the scale similarity model. The decomposition in (8) can also be interpreted as breaking $\mathbf{B}$ into its slow and rapid varying parts—relative to the time scale of its response to variations in the mean flow [20]. In MILES, the rapid part that cannot be captured by isotropic models relates to $\mathbf{B}^{(2)}$, while the slow part relates to $\mathbf{B}^{(1)}$. Borue and Orszag [21] have shown that a $\mathbf{B}^{(2)}$ type term improves the correlations between the exact and modeled SGS stress tensor. A closely-related view further explaining the effectiveness of ILES formulations based on local monotonicity (or sign) preservation concepts has been given by Margolin and Rider [18]; they argued that the leading order truncation error introduced by NFV algorithms represents a physical flow regularization term, providing necessary modifications to the governing equations that arise when the motion of *observables*—finite volumes of fluid convected over finite intervals of time—is considered.

Detailed properties of the implicit SGS model are related to the flux limiter Γ and to the choice of low- and high-order schemes; they also relate as well to other specific features of the scheme—e.g., such as monotonicity, l_1-contraction, local monotonicity preservation, and griding. We have illustrated above in (8) and discussed elsewhere [13, 14] how some of these properties can directly affect the implicit SGS modeling effectiveness in the MILES context. MILES performance as a function of flux limiter is discussed further below; dependence on the choice of low order scheme has been examined in Ref. [22].

In what follows we address effects of variations in the flux-limiter Γ. To this end we consider first high-resolution schemes that can be formulated using the ratio of consecutive gradients,

$$r = \frac{\delta\mathbf{v}^n_{P-1/2}}{\delta\mathbf{v}^n_{P+1/2}} = \frac{(\mathbf{v}^n_P - \mathbf{v}^n_{P-1})}{(\mathbf{v}^n_{P+1} - \mathbf{v}^n_P)}.$$

Examples of well-known flux-limiters that fit into this category are:

1. the minmod flux-limiter of Roe, e.g. [23], with
$$\Gamma = \max\big(0, \min(1, r)\big),$$
2. the van-Leer flux-limiter, e.g. [23], with
$$\Gamma = \frac{r + |r|}{1 + |r|},$$
3. the superbee flux-limiter, Roe, e.g. [23], with
$$\Gamma = \max\big(0, \max\big(\min(2r, 1), \min(r, 2)\big)\big),$$

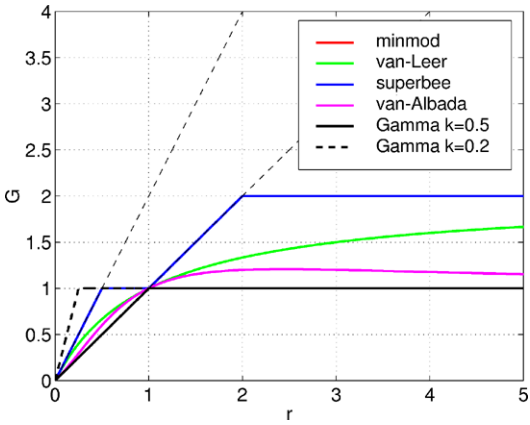

Fig. 2 TVD regions for first and second order accurate TVD schemes together with selected limiters

4. the van-Albada flux-limiter, e.g. [24], with

$$\Gamma = \frac{r + r^2}{1 + r^2},$$

5. the GAMMA flux-limiter, e.g. [25], with

$$\Gamma = \frac{1-k}{k} r \left[\theta(r) - \theta\left(r - \frac{k}{1-k} \right) \right] + \theta\left(r - \frac{k}{1-k} \right),$$

where k is a parameter of the scheme such that $k \in [0, 1]$, and θ is the Heaviside function. Note that when $k = 0.5$ this scheme becomes TVD.

Some of these limiters are compared in Fig. 2 together with the r-independent limiting cases—the first-order upwind (UD, $\Gamma = 0$) and the second-order central difference (CD, $\Gamma = 1$) schemes. In Fig. 2 the TVD constraint

$$\mathrm{TV}\left(\mathbf{v}^{n+1}\right) \leq \mathrm{TV}\left(\mathbf{v}^{n}\right), \quad \text{where } \mathrm{TV}\left(\mathbf{v}^{n}\right) = \sum_{P} \left\| \mathbf{v}^{n}_{P+1} - \mathbf{v}^{n}_{P} \right\|,$$

reformulated as $0 \leq |\Gamma(r), \Gamma(r)/r| \leq 2$ [23] is satisfied in the region bounded by the traces associated with the minmod and superbee limiters, which includes the van-Leer, van-Albada and ($k = 0.5$) GAMMA limiters. The diffusivity decreases as the flux-limiters approach that of the superbee limiter, which results in the least diffusive scheme.

We can also consider other high-resolution schemes, such as FCT [26] and PPM [27], which can also use a similar flux-limiting type formalism based on $\mathbf{v}_f = \mathbf{v}_f^H - (1 - \Gamma)[\mathbf{v}_f^H - \mathbf{v}_f^L]$, but for which the flux limiter cannot simply be formulated in terms of the ratio of consecutive gradients, r. In the present study we have however only included the FCT-limiter [26]. Some of these schemes (e.g. FCT, PPM) are locally monotonicity-preserving, i.e. given the solution $\mathbf{v}_P^{n+1} = H(\mathbf{v}^n_{P-k}, \mathbf{v}^n_{P-k+1}, \ldots, \mathbf{v}^n_{P+k})$ then if $\mathbf{v}^0_P \geq \mathbf{v}^0_{P+1}$ then $\mathbf{v}^n_P \geq \mathbf{v}^n_{P+1}$ for all P and n.

The global performance of MILES as a function of flux-limiter is documented in Fig. 3, showing studies of fully developed turbulent channel flow at a friction velocity based Re-number of $Re_\tau = 590$, compared with DNS results [27]. The channel

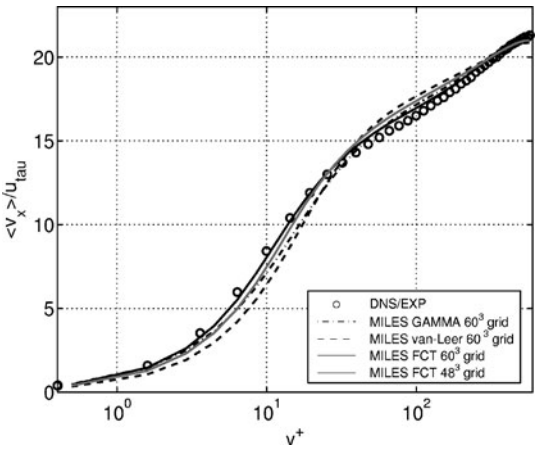

Fig. 3 MILES of $Re_\tau = 590$ channel flow; dependence on choice of flux-limiter

flow calculations will be discussed in detail below, and are carried out on 60^3 and 48^3 grids with uniform spacing the streamwise and spanwise directions. Periodic boundary conditions are employed in both streamwise and spanwise directions, together with no-slip conditions in the wall-normal directions. The influence of the flux limiter is comparatively small but has been observed to be sensitive to the wall-normal resolution (cf. [28]). From this comparison it is evident that the van-Leer limiter is too diffusive, producing poor velocity profiles, while both FCT and GAMMA produce velocity profiles that agree well with the reference DNS data. Reported ILES work surveyed in [12] involved a broad range of NFV methods, including among others, use of locally-monotonicity-preserving FCT [13, 14] and PPM-based studies of homogeneous turbulence [29], locally-sign-preserving MP-DATA [18], TVD-based turbulence studies [30], and studies of channel flows using Godunov's exact Riemann solver [31]. The following section discusses applications involving FCT-based MILES.

5 MILES Applications

The first category of applications discussed below comprises what we regard to be the traditional Computational Fluid Dynamics (CFD) role. For these cases, laboratory experiments can be carried out exhibiting the effects of flow dynamics and instabilities—typically demonstrating only the end outcome of complex three-dimensional (3D) physical processes. Time-dependent experiments based on numerical simulations with precise control of initial and boundary conditions, are ideally suited to supplement these laboratory studies, providing insights into the underlying flow dynamics and topology. Three groups of such examples are provided: (i) canonical flows to demonstrate MILES benchmark studies; (ii) mixing layer and jet flows to demonstrate MILES ability to capture complex flow physics; (iii) external flows to demonstrate the MILES ability to deal with moderately complex geometries.

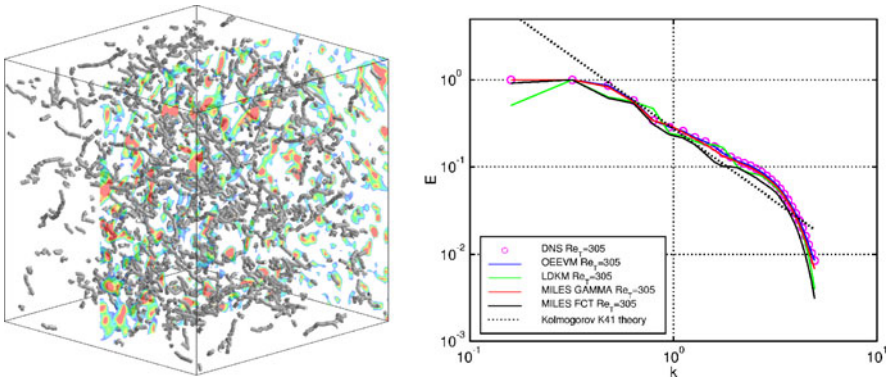

(**a**) (**b**)

Fig. 4 Forced homogeneous isotropic turbulence: (**a**) iso-surfaces of Q; (**b**) energy spectra

5.1 Canonical Cases

MILES of free shear flows have been extensively benchmarked and/or compared with laboratory flows in various different flow configurations at moderately-to-high *Re* numbers. Recent studies of forced and decaying homogeneous isotropic turbulence, studies of wakes, subsonic and supersonic mixing layers, jet flows, and channel flows demonstrated that MILES can be successfully used to simulate (and elucidate) the governing features of the unsteady flow dynamics. Selected representative examples are discussed in what follows.

5.1.1 Forced Homogeneous Turbulence

First, we consider forced homogeneous isotropic turbulence for a Taylor *Re*-number of $Re_T = 96$ at 32^3 and 64^3 resolution, for which DNS data is available [19]. The body force, $\mathbf{f}$, is here used to create random forcing of the large scales. For this purpose we use the forcing scheme of Eswaran and Pope [32], to drive the largest flow scales, see [33] for further details. The initial velocity field $\bar{\mathbf{v}} = \bar{\mathbf{v}}(\mathbf{x}, 0)$ is created by superimposing Fourier modes, having a prescribed energy spectrum but random phases.

Figure 4(a) shows typical visualizations at 64^3 resolution of the second invariant of the velocity gradient, i.e., $Q = \frac{1}{2}(\|\bar{\mathbf{W}}\|^2 - \|\bar{\mathbf{D}}\|^2)$. The observed vortical structure implies that weak and strong vortices have different topologies while there is no evident structure in the lower intensity regions. The higher intensity regions tend to be organized in slender tubes or elongated filaments as found with other LES studies. The vortical structures predicted by LES are considerably thicker than those obtained by DNS. However, filtering the DNS data results in thicker vortical structures, qualitatively very similar to those obtained by the LES. It is virtually impossible to distinguish between different SGS models by inspecting such visualizations,

but by comparing Probability Density Functions (PDFs) of, e.g., the resolved vorticity magnitude $|\bar{\omega}|$ (not shown) we find that MILES and LDKM [33, 34] result in somewhat larger fractions of small-scale vorticity than conventional eddy-viscosity models such as the OEEVM [15].

Figure 4(b) presents the time-averaged energy spectra for the $Re_T = 305$ case at 64^3 resolution together with a DNS spectrum [19] and the theoretical model spectrum of Driscoll and Kennedy [35]. The energy spectra are found to depend on the effects of the LES models only towards the high wavenumber end of the inertial range, and into the viscous subrange. A larger fraction of the turbulence is resolved in the 64^3 case as compared to the 32^3 results, and hence the influence of the SGS model is comparatively smaller in the former case. In general, we find that the spectra from MILES and LDKM are in better agreement with DNS data than, e.g., the OEEVM, at high wavenumbers.

5.1.2 Turbulent Channel Flow

Next we focus on fully developed turbulent channel flow at (bulk) *Re*-numbers between $Re = 15{,}000$ and 400,000. The channel of length $6h$ and width $3h$ is confined between two parallel plates $2h$ apart, where h is the channel half-width. The flow is driven by a fixed mass flow in the streamwise ($\mathbf{e}_x$) direction. We use no-slip conditions in the cross-stream ($\mathbf{e}_y$) direction and periodic conditions in the ($\mathbf{e}_x$) and spanwise ($\mathbf{e}_z$) directions. The friction velocity is $u_\tau = \sqrt{\tau_w}$, where τ_w is the wall-shear stress. We vary the mass flow to obtain three target friction-velocity-based *Re* numbers: $Re_\tau \approx 395$, 2000, and 10,000 (the first corresponds to the DNS data [27], and the second to the laboratory data [36]). The grid consists of 60^3 cells with uniform spacing in the stream- and spanwise directions, whereas we use geometrical progression in the $\mathbf{e}_y$-direction to appropriately cluster the grid near the walls to resolve the velocity gradients.

Figure 5(a) shows the main channel flow features in terms of vortex lines, contours of the streamwise velocity component $\bar{v}_x$ and isosurfaces of the second invariant of the velocity gradient Q. By correlating isosurfaces of Q with the velocity fluctuations close to the wall, we found that vortices above the low-speed streaks are often ejected away from the wall, producing hairpin vortices stretched by the ambient shear. Using this mechanism, vorticity produced in the viscous region is advected into the boundary layer, making it turbulent. The spanwise resolution appears more important for accurate large-scale-dynamics prediction than the streamwise resolution. The wall-normal resolution is critical for the correct wall-shear stress τ_w prediction, which, in turn, is important for making correct estimates of, for example, the drag.

In Fig. 5(b), we compare LES mean velocity $\langle \bar{v}_x \rangle$ predictions (integrated over time, x, and z) with DNS data [27] and experimental data [36]. For $Re_\tau = 395$, all LES models used show very good agreement with the DNS data. When the flow is well resolved, the SGS model details are of little importance to the resolved flow, because most of the energy (about 98 percent) and structures are resolved on the

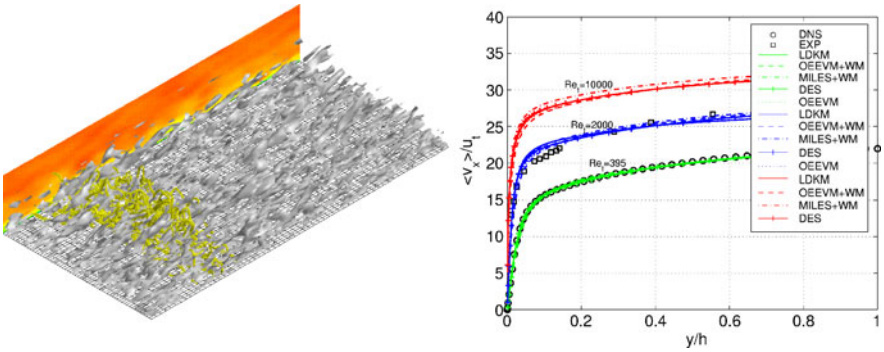

Fig. 5 Fully developed channel flow: (**a**) instantaneous visualization in terms of contours of $\bar{v}_x$, vortex lines, and isosurfaces of Q; (**b**) vertical profiles of mean streamwise velocity $\langle \bar{v}_x \rangle$

grid. For $Re_\tau \approx 1800$, we still see good agreement between LES and experimental data, but with somewhat larger scatter in the LES data. This case is well resolved, with about 87 percent of the energy belonging to the resolved scales. We do not have any data to compare with, for $Re_\tau = 10{,}000$, but we may compare it (asymptotically) with the lower Re_τ number velocity profiles and the log law. The scatter among the LES models is now larger, and we find that the best agreement with the log law is obtained by using Detached Eddy Simulation (DES) [37] and the localized dynamic (LDKM) subgrid turbulence model [34] followed, in turn, by MILES+WM, OEEVM+WM [38] and OEEVM [15] where WM denotes the wall model [38]. However, for the second order statistical moments, MILES+WM and OEEVM+WM provide better agreement with data.

The eddy-viscosity models are successful because ν_k responds to energy accumulation in the small scales by adjusting the dissipation before it contaminates the resolved scales. MILES performs well because it mimics the resolved flow anisotropies. MILES turns out also to be computationally competitive, with typical work figures of OEEVM = 1.00, MILES = 0.95, OEEVM+WM = 1.05, DES = 1.10, and LDKM = 1.15.

5.2 Free Shear Flows: Global Instabilities and Vorticity Dynamics

Characterizing the local nature of free-shear-flow instabilities and their global nonlinear development in space and time is of fundamental importance for practical shear-flow control. Linear inviscid stability analyses have shown the convectively unstable nature of the spatially evolving subsonic mixing layer with respect to vortical fluctuations. Consequently, except in rare configurations with global-absolute instabilities, we expect environmental disturbances to drive turbulent mixing layers; self-sustained instabilities have generally not been expected. Mechanisms influenc-

ing re-initiation of the instabilities and transition to turbulence in free-shear flows are:

- disturbances in the free streams,
- disturbances due to boundary layers, wakes, small recirculation zones, or acoustic environmental disturbances, and
- disturbances fed back from downstream events in the flow.

Isolating these mechanisms is difficult because turbulence in free streams and boundary layers cannot be eliminated. Numerical simulations of spatially evolving shear flows can be essentially eliminated, the first two disturbances and the third can be addressed through careful control of the imposed boundary conditions.

5.2.1 Global Instabilities in Free Flows

An important question is whether a free mixing layer can be globally unstable with the self-excitation upstream induced by pressure disturbances generated via finite-amplitude fluid accelerations downstream. A previous study successfully addressed this question with FCT based MILES of spatially evolving flows [39]. Numerical simulations of compressible, subsonic, planar shear-flows were used to investigate the role of feedback in the re-initiation of the vortex roll-up. The study dealt with unforced, spatially evolving mixing layers for which the acoustic disturbance propagation can be appropriately resolved; and boundary effects were ensured to be negligible. The simulation shows global self-sustaining instabilities, in which new vortex roll-ups were triggered in the initial shear layer by pressure disturbances originating in the fluid accelerations downstream. This re-initiation mechanism, absent in linear treatments of stability, was demonstrated conclusively and examined as a function of Mach number and free-stream velocity ratio.

Another study demonstrated similar self-excited global instabilities in supersonic, countercurrent jets, based on upstream feedback mechanisms acting on the subsonic outer jet regions (see Fig. 6) [40]. Recognition of these global instabilities provided new insights to explain previously unresolved discrepancies between laboratory and theoretical studies, suggesting practical approaches to active control of these jets. A key computational capability used in both of these global instability studies was the ability to isolate the generation of propagation of acoustical disturbances correlated with the large-scale vortex dynamics. Relevant features accurately captured with MILES included the quadrupole pattern of acoustic production associated with vortices, the significantly more intense dilatation and pressure fluctuations associated with vortex pairing, as well as the very low fluctuation levels involved (for example, four orders of magnitude smaller than ambient values [39, 40]).

Accurate resolution of the small characteristic fluctuation levels, typically associated with acoustical radiation from flow accelerations, involves major challenges:

- Complex vortex dynamics associated with acoustical production must be captured.

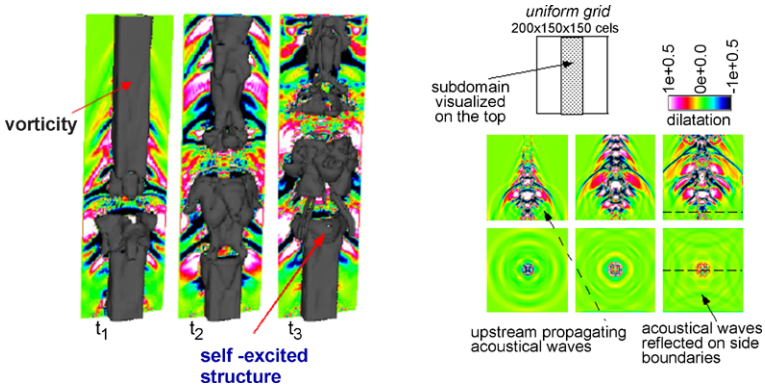

Fig. 6 MILES studies of global instabilities in a countercurrent supersonic cold square jet in terms of instantaneous visualizations [40]

- The numerical algorithm's dispersiveness should be minimized to ensure good modeling of the acoustical propagation properties of the small wavelengths.
- Because of the very small energy of the acoustic field compared to that of the flow field, there is a potential for spurious sound sources due to numerical discretization.

Because of the tensorial nature of its implicit SGS model, and the inherently low numerical diffusion involved, the use of flux limiting in MILES offers an overall effective computational alternative to conventional SGS models in this context. MILES was used to extensively investigate the natural mechanisms of transition to turbulence in rectangular jets evolving from laminar conditions [41], in compressible (subsonic) jet regimes with aspect ratio $AR = 1$ to 4 and moderately high Re. The studies demonstrated qualitatively different dynamical vorticity geometries characterizing the near jet, involving

- self-deforming and splitting vortex rings,
- interacting ring and braid (rib) vortices, including single ribs aligned with corner regions ($AR \geq 2$), and rib pairs (hairpins) aligned with the corners ($AR = 1$), and,
- a more disorganized flow regime in the far jet downstream, where the rotational fluid volume is occupied by a relatively weak vorticity background with strong, slender tube-like filament vortices filling a small fraction of the domain.

Figure 7(a) illustrates characteristic axis-switching and bifurcation phenomena from visualizations of laboratory elliptical jets subject to strong excitation at the preferred mode [42, 43]. We compare it to the carefully developed simulation results (see Figs. 7(b) and 7(c)) designed to address unresolved issues in vortex dynamics. Detailed key aspects—namely, reconnection, bridging, and threading (see Fig. 7(b))—could not be captured in the laboratory studies and were first demonstrated by the simulations.

Jet flows develop in different possible ways, depending on

- their particular initial conditions,

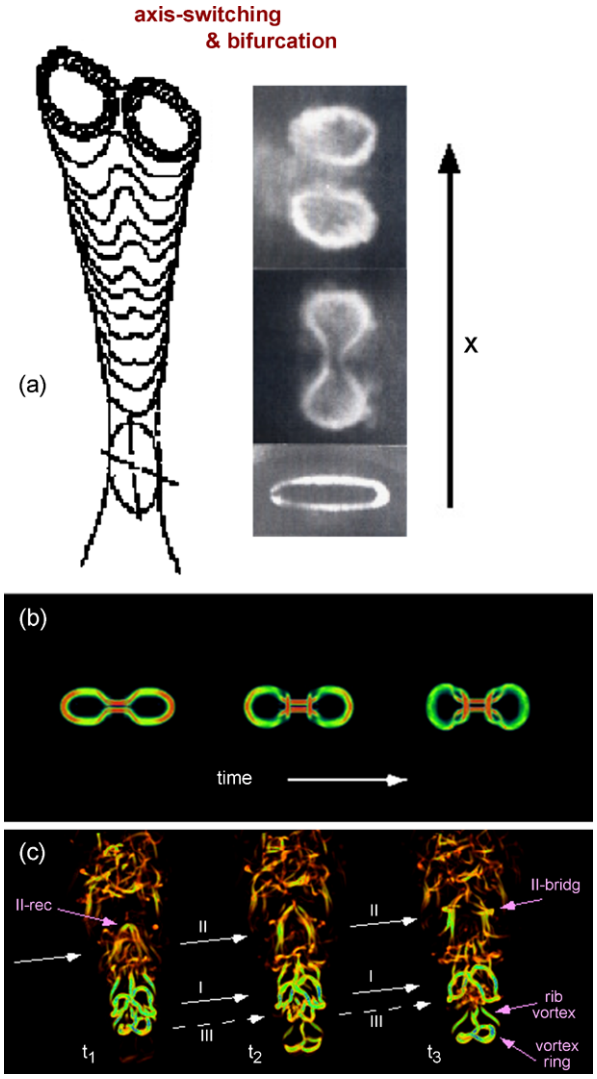

Fig. 7 Vortex dynamics and transition to turbulence in subsonic noncircular jets; (**a**) laboratory studies [42, 43], (**b**) and (**c**) detailed vortex dynamics elucidated by simulations [41]

- nozzle geometry and modifications introduced at the jet exit,
- the types of unsteady vortex interactions initiated, and
- local transitions from convectively to absolutely unstable flow.

Taking advantage of these flow control possibilities is of interest to improve the mixing of a jet, or plume, with its surroundings in practical applications demanding:

- enhanced combustion between injected fuel and background oxidizer,
- rapid initial mixing and submergence of effluent fluid,
- less intense jet noise radiation,
- reduced infrared plume signature.

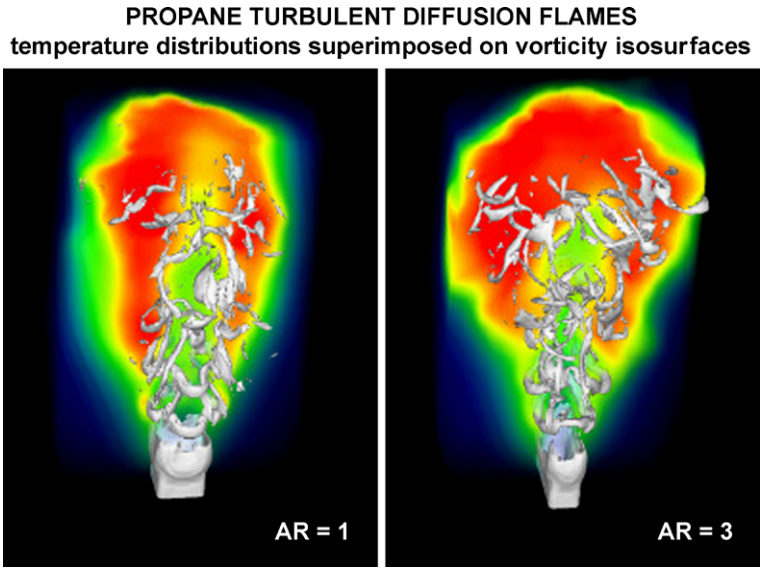

Fig. 8 Visualizations of non-premixed combustion regions as a function of aspect ratio [41]. Temperature distributions (*color*) in the back half of the visualized subvolume are superimposed to isosurfaces of the vorticity magnitude (*gray*)

For example, the jet entrainment rate—the rate at which fluid from the jet becomes entangled or mixed with that from its surroundings—can be largely determined by the characteristic rib-ring coupling geometry and the vortex-ring axis-switching times (see Fig. 8) [40].

5.3 Moderately Complex Geometry: Flow Over a Prolate Spheroid

Crucial additional issues of LES of inhomogeneous high-*Re* flows to be addressed relate to boundary condition (supergrid) modeling and overall computational model validation [42, 43]. From the practical point of view, it is of utmost importance to consider how the non-linear combination of all—algorithmic, physics-based, SGS, and supergrid—aspects of the model affect the simulation of complex systems for which detailed DNS-type approaches are not possible and for which only limited experimental data might be available at best.

Despite its simple geometry, the flow around a prolate spheroid at an incidence (see Fig. 6(a)) contains a rich gallery of complex 3D flow features. These include:

- stagnation flow,
- 3D boundary layers under influence of pressure gradients and streamline curvature
- cross-flow separation, and
- the formation of free vortex sheets producing streamwise vortices.

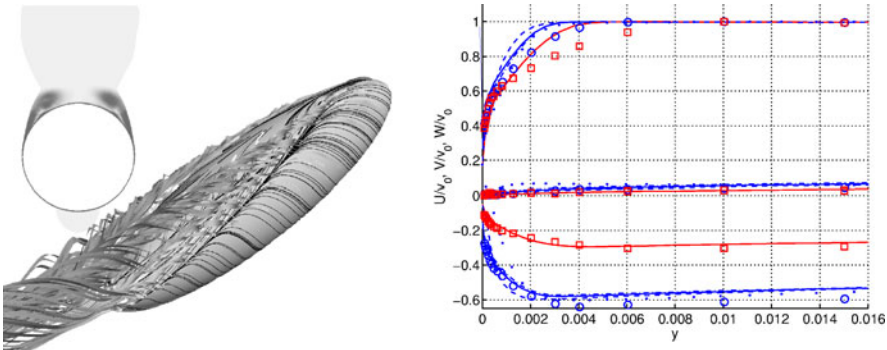

Fig. 9 Flow around a prolate spheroid: (**a**) perspective view and contours of the vorticity magnitude $|\omega|$ at $x/L = 0.772$; (**b**) velocity comparison at $x/L = 0.772$ and $\varphi = 60°$ between experimental (○ and □) and predicted data at $\alpha = 10°$ (*black*) and $\alpha = 20°$ (*gray*). (—) OEEVM+WM on grid A, (- - -) MILES+WM on grid A, (-.-.) LDKM on grid A, (· · · ·) LDKM on grid B and (· · ·) DES on grid A

These features are archetypes of flows over more complicated airborne and underwater vehicles warranting in-depth study. Previously [42, 43] we studied the flow around a 6 : 1 prolate spheroid mounted in a wind tunnel with a rectangular cross-section [44] at $\alpha = 10°$ and 20° angles of attack. Based on the free-stream velocity v_0 and the body length L, the Re number is $Re_L = 4.2 \cdot 10^6$. The domain is discretized with a block-structured mesh, supported by a double O-shaped block structure. Two meshes are used in order to parameterize effects of the grid on the boundary layer resolution. Mesh A has $0.75 \cdot 10^6$ cells and $y^+ \approx 25$ and mesh B has $1.50 \cdot 10^6$ cells with $y^+ \approx 5$. At the inlet, $\bar{\mathbf{v}} = v_0\mathbf{n}$ and $\partial\bar{p}/\partial n = 0$, where $\mathbf{n}$ is the outward pointing unit normal, and at the outlet $\bar{p} = p_\infty$ and $\partial(\bar{\mathbf{v}} \cdot \mathbf{n})/\partial n = 0$. On the body, no-slip conditions are used.

Figure 9(a) shows perspective views from the port side of the prolate spheroid at $\alpha = 20°$. The flow is represented by surface streamlines, stream-ribbons, and contours of the vorticity magnitude $|\bar{\omega}|$ at $x/L = 0.772$, where $\bar{\omega} = \frac{1}{2}\nabla \times \bar{\mathbf{v}}$ is the vorticity. The stream-ribbons show the complexity of the flow. On the windward side, an attached 3D boundary layer is formed, while on the leeward side, the flow detaches from the hull—because of the circumferentially adverse pressure gradient, and rolls up into a counterrotating pair of longitudinal spiraling vortices on the back of the body. Furthermore, fluid from the windward side is advected across the spheroid, engulfed into the primary vortices and subsequently ejected into the wake.

Figure 9(b) shows the time-averaged velocity components (U, V, W) at $x/L = 0.772$ and at $\varphi = 90°$. The velocity components are presented in the body-surface coordinate system [44]. For V and W, we see good agreement between predictions and measurements for all models—with DES providing the least accurate comparison. We obtained the best agreements with OEEVM and MILES with a wall-model [38] on grid A (OEEVM+WM and MILES+WM). Concerning U, we found significant differences as a function of the various models and grid resolu-

tions. We found best agreements for MILES+WM and OEEVM+WM, whereas the LDKM and DES predictions show larger deviations from the experimental data. The LDKM appears to require better resolution than what we have provided because it underpredicts the boundary layer thickness. The results from MILES+WM and OEEVM+WM appear virtually unaffected by resolution, which is expected because the wall model is designed to take care of the errors introduced by poor resolution in the boundary layer. Also interesting is that the effects of changing the angle of attack α—very important when studying, for example, maneuvering—are very well reproduced in the simulations.

5.4 Challenging New Role of Simulations

For the studies of submarine hydrodynamics and flows in urban areas discussed separately in this volume [22], it is unlikely that we will ever have a deterministic predictive framework based on computational fluid dynamics. This is due to the inherent difficulty in modeling and validating all the relevant physical sub-processes and acquiring all the necessary and relevant boundary condition information. On the other hand, these cases are representative of very fundamental ones for which whole-domain scalable laboratory studies are impossible or very difficult, but for which it is also crucial to develop predictability.

5.4.1 Submarine Hydrodynamics

The flow around a submarine is extremely complicated and characterized by very high Re, $O(10^9)$. Full-scale experiments are complicated and very expensive and are of limited value due to the difficult measurement settings. RANS of full-scale submarine hydrodynamics are barely within reach, whereas LES is currently out of reach due to the wide range of scales present. For model-scale situations ($Re \approx 10^7$), it might be possible to conduct LES and DES [45]. In particular, if we're interested in vortex dynamics, flow noise, and the coupling between the propeller dynamics and the flow around the hull, LES and DES are our only alternatives for the foreseeable future.

As Fig. 7(a) shows, each appendage generates a wake and several vortex systems. A horseshoe-vortex pair is formed in the junction between the hull and the appendage, whereas a tip-vortex pair is formed at the tip of the appendage. Additional vortex systems can be formed, e.g., on the side of the sail towards the trailing edge or in the boundary layer of the tapered sections of the hull. These vortex systems can interact with each other and with the (unsteady) boundary layer to form a very complex flow entering the propeller, thus causing vibrations and noise. In addition, the ocean water is usually stratified, with density variations caused by differences in temperature and salinity between ocean currents, or between the surface water and deeper water. Stratification influences the turbulence and the large flow

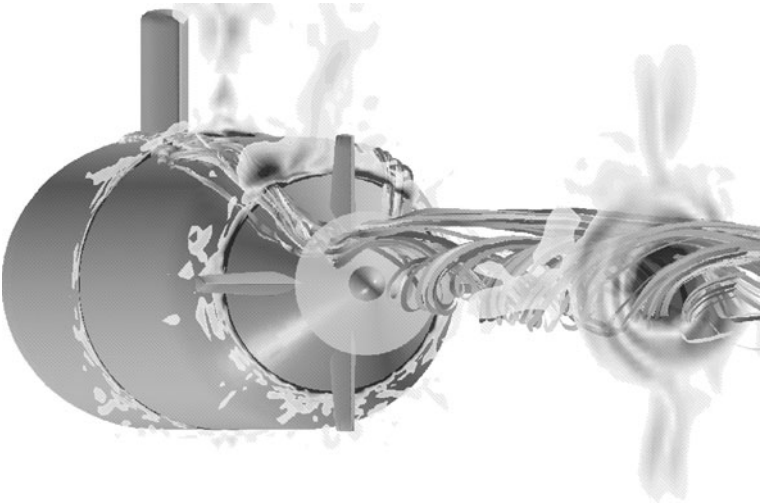

Fig. 10 Submarine hydrodynamics: the main flow features represented by stream-ribbons and contour plots of the vorticity magnitude in three cross-sections

structures in the wake, typically resulting in horizontally flattened flow structures (so-called pancake vortices), which would not occur in nonstratified waters.

The case discussed here is the fully appended DARPA Suboff configuration [46] constructed from analytical surfaces, and shown in Fig. 10. Experimental data, using hot-film techniques, are provided at $Re = 12 \cdot 10^6$ based on the overall hull length L, the free-stream velocity u_0 and ν [47]. The total measurement uncertainty in the velocity data—i.e., the geometrical mean of the bias and precision errors, is estimated to be about 2.5% of u_0. The computational domain consists of the submarine model mounted in a cylinder having the same hydraulic diameter as the wind tunnel used in the scale model experiments. The cylinder extends one hull-length upstream and two hull-lengths downstream, thus being $4L$ in overall length. For the hull an O-O topology is used, while for the sail and stern appendages C-O topologies are used and care is taken to ensure that the cell spacings and aspect ratios are suitable for capturing the boundary layers along the hull.

Typically, about 20 cells are contained within the thickness of the boundary layer on the parallel midsection of the hull, having a typical wall distance for the first cell $y^+ \approx 8$. Two grids of about $3 \cdot 10^6$ and $6 \cdot 10^6$ nodes were used. At the inlet boundary, $\bar{\mathbf{v}} = u_0\mathbf{n}$ and $(\nabla \bar{p} \cdot \mathbf{n}) = 0$, at the outlet $\bar{p} = p_0$ and $(\nabla \bar{\mathbf{v}}) \cdot \mathbf{n} = \mathbf{0}$, whereas free-slip conditions are used at the wind-tunnel walls, and no-slip conditions are used on the hull. All LES are initiated with quiescent conditions and the unsteady flow in LES is allowed to evolve naturally (i.e., without any external forcing).

In Figs. 11(a) and 11(b) we show typical comparisons between predictions of towed and self-propelled cases and experimental data [47] of the distribution of the time-averaged static pressure coefficient $C_P = 2(\langle \bar{p} \rangle - p_0)/u_0^2$ along the meridian line of hull and of the circumferentially averaged velocity in the propeller plane. Very good agreement between the measurement data and the computations is ob-

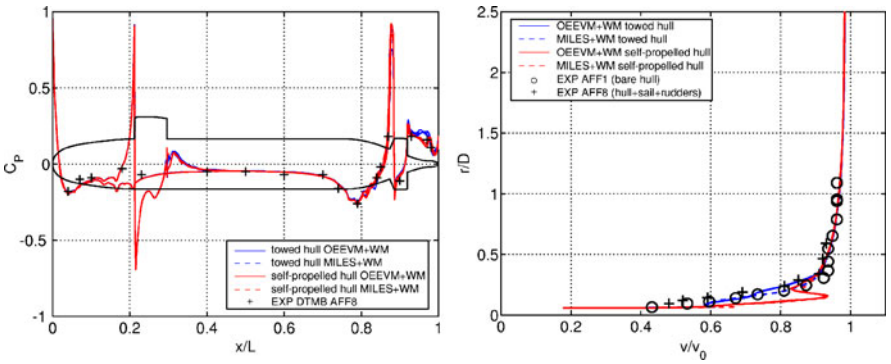

(**a**) (**b**)

Fig. 11 Submarine hydrodynamics: comparison of the mean pressure and mean velocity: (**a**) along the meridian line of the hull; (**b**) in the propeller plane

served along the entire hull section for the towed case. Virtually no differences in the C_P distribution can be observed between the towed and the self-propelled cases—with the exception of the far-end of the tapered section of the stern, nor do we see significant differences between the MILES+WM and LDKM predictions. Concerning the velocity distributions, the differences are attributed to the presence of the propeller (or rather the actuator-disc used to model the effects of the propeller), and show the effects of the axial pressure gradient, as implicitly imposed by the propeller causing a suction effect along the stern part of the hull. Based on the secondary velocity vector field (not shown) the location of the horseshoe-vortex pair is estimated in the case of the towed case from predictions (measurements) to be at $r/R \approx 0.41$ (0.38) and $\varphi \approx \pm 23°$ ($\pm 22°$), respectively.

6 Outlook

In the absence of an accepted universal theory of turbulence, the development and improvement of SGS models are unavoidably pragmatic and based on the rational use of empirical information. Classical approaches have included many proposals ranging from inherently limited eddy-viscosity formulations to more sophisticated and accurate mixed models. The main drawback of mixed models relates to their computational complexity, and ultimately, to the fact that well-resolved (discretization-independent) LES is prohibitively expensive for the practical flows of interest at moderate-to-high *Re*. This has recently led many researchers to abandon the classical LES formulations, shifting their focus directly to the SGS modeling implicitly provided by nonlinear stabilization achieved algorithmically, through the use of a particular class of numerical schemes, or based on regularization of the discretization of conservation laws.

In ILES (MILES), the effects of SGS physics on the resolved scales are incorporated in the functional reconstruction of the convective fluxes using NFV meth-

ods. Analysis based on the modified equations shows that ILES provides implicitly implemented anisotropic SGS models dependent on the specifics of the particular numerical scheme—i.e., on the flux limiter, on the choice of low- and high-order schemes, and on the griding. By focusing on the inviscid inertial-range dynamics and on regularization of the underresolved flow, ILES follows up very naturally on the historical precedent of using this kind of numerical schemes for shock capturing. Challenges for ILES include constructing a common appropriate mathematical and physical framework for its analysis and development, further understanding the connections between implicit SGS model and numerical schemes, and, in particular, how to address building physics into the numerical scheme to improve global ILES performance, i.e., on the implicitly-implemented SGS dissipation & backscatter features. Moreover, additional (explicit) SGS modeling might be needed to address inherently small-scale physical phenomena such as scalar mixing and combustion—which are actually outside the realm of any LES approach: how do we exploit the implicit SGS modeling provided by the numerics, to build "efficient mixed" (explicit/implicit) SGS models?

Acknowledgements This work was completed while one of us (FFG) was the 2003–2004 Orson Anderson Distinguished Visiting Scholar at the Los Alamos National Laboratory, on Sabbatical leave from the Naval Research Laboratory in Washington DC. Support from the Office of Naval Research through the Naval Research Laboratory 6.1 Computational Physics task area is also greatly appreciated.

References

1. Sagaut, P.: Large Eddy Simulation for Incompressible Flows. Springer, New York (2002)
2. Liu, S., Meneveau, C., Katz, J.: On the properties of similarity subgridscale models as deduced from measurements in a turbulent jet. J. Fluid Mech. **275**, 83 (1994)
3. Bardina, J.: Improved turbulence models based on large eddy simulation of homogeneous incompressible turbulent flows. Ph.D. Thesis, Stanford University (1983)
4. Adams, N.A., Stolz, S.: Deconvolution methods for subgrid-scale approximation in LES. In: Geurts, B.J. (ed.) Modern Simulation Strategies for Turbulent Flows, p. 21. Edwards, Philadelphia (2001)
5. Spalart, P.R., Jou, W.H., Strelets, M., Allmaras, S.R.: Comments on the feasibility of LES for wings, and on hybrid RANS/LES approach. In: Advances in DNS/LES, First AFOSR International Conference in DNS/LES. Greyden Press, Columbus (1997)
6. Boris, J.P.: On large eddy simulation using subgrid turbulence models. In: Lumley, J.L. (ed.) Whither Turbulence? Turbulence at the Crossroads, p. 344. Springer, New York (1989)
7. Boris, J.P., Grinstein, F.F., Oran, E.S., Kolbe, R.J.: New insights into large eddy simulations. Fluid Dyn. Res. **10**, 199 (1992)
8. J. Fluids Eng. **124**(4) (2002). Alternative LES and Hybrid RANS/LES, edited by F.F. Grinstein and G.E. Karniadakis, pp. 821–942
9. Int. J. Numer. Methods Fluids **39**(9) (2002). Special Issue edited by D. Drikakis, pp. 763–864
10. von Neumann, J., Richtmyer, R.D.: A method for the numerical calculation of hydrodynamic shocks. J. Appl. Phys. **21**, 232 (1950)
11. Smagorinsky, J.: The beginnings of numerical weather prediction and general circulation modeling: early recollections. Adv. Geophys. **25**, 3 (1983)
12. Grinstein, F.F., Margolin, L.G., Rider, W.J. (eds.): Implicit Large Eddy Simulation: Computing Turbulent Flow Dynamics, 2nd edn. Cambridge University Press, New York (2010)

13. Fureby, C., Grinstein, F.F.: Monotonically integrated large eddy simulation of free shear flows. AIAA J. **37**, 544 (1999)
14. Fureby, C., Grinstein, F.F.: Large eddy simulation of high Reynolds number free and wall bounded flows. J. Comput. Phys. **181**, 68 (2002)
15. Schumann, U.: Subgrid scale model for finite difference simulation of turbulent flows in plane channels and annuli. J. Comput. Phys. **18**, 376 (1975)
16. Carati, D., Winckelmans, G.S., Jeanmart, H.: Exact expansions for filtered scales modeling with a wide class of LES filters. In: Voke, P.R., Sandham, N.D., Kleiser, L. (eds.) Direct and Large Eddy Simulation III, pp. 213–224. Kluwer Academic, Dordrecht (1999)
17. Godunov, S.K.: Reminiscences about difference schemes. J. Comput. Phys. **153**, 6–25 (1999)
18. Margolin, L.G., Rider, W.J.: A rationale for implicit turbulence modeling. Int. J. Numer. Methods Fluids **39**, 821 (2002)
19. Jimenez, J., Wray, A., Saffman, P., Rogallo, R.: The structure of intense vorticity in isotropic turbulence. J. Fluid Mech. **255**, 65 (1993)
20. Shao, L., Sarkar, S., Pantano, C.: On the relationship between the mean flow and subgrid stresses in large eddy simulation of turbulent shear flows. Phys. Fluids **11**, 1229 (1999)
21. Borue, V., Orszag, S.A.: Local energy flux and subgrid-scale statistics in three dimensional turbulence. J. Fluid Mech. **366**, 1 (1998)
22. Patnaik, G., Boris, J.P., Grinstein, F.F., Iselin, J.P.: Large scale urban simulations with FCT, Chap. 4 in this volume; see also Chap. 17 in Ref. [12] (2004)
23. Hirsch, C.: Numerical Computation of Internal and External Flows. Wiley, New York (1999)
24. Albada, G.D., van Leer, B., van Roberts, W.W.: A comparative study of computational methods in cosmic gas dynamics. Astron. Astrophys. **108**, 76 (1982)
25. Jasak, H., Weller, H.G., Gosman, A.D.: High resolution NVD differencing scheme for arbitrarily unstructured meshes. Int. J. Numer. Methods Fluids **31**, 431 (1999)
26. Boris, J.P., Book, D.L.: Flux corrected transport I, SHASTA, a fluid transport algorithm that works. J. Comput. Phys. **11**, 38 (1973)
27. Colella, P., Woodward, P.: The piecewise parabolic method (PPM) for gas dynamic simulations. J. Comput. Phys. **54**, 174 (1984)
28. Moser, R.D., Kim, J., Mansour, N.N.: Direct numerical simulation of turbulent channel flow up to $Re_\tau = 590$. Phys. Fluids **11**, 943 (1999)
29. Porter, D.H., Pouquet, A., Woodward, P.R.: Kolmogorov-like spectra in decaying three-dimensional supersonic flows. Phys. Fluids **6**, 2133 (1994)
30. Garnier, E., Mossi, M., Sagaut, P., Comte, P., Deville, M.: On the use of shock-capturing schemes for large eddy simulation. J. Comput. Phys. **153**, 273 (2000)
31. Okong'o, N., Knight, D.D., Zhou, G.: Large eddy simulations using an unstructured grid compressible Navier-Stokes algorithm. Int. J. Comput. Fluid Dyn. **13**, 303 (2000)
32. Eswaran, V., Pope, S.B.: An examination of forcing in direct numerical simulation of turbulence. Comput. Fluids **16**, 257 (1988)
33. Fureby, C., Tabor, G., Weller, H., Gosman, D.: A comparative study of sub grid scale models in isotropic homogeneous turbulence. Phys. Fluids **9**, 1416 (1997)
34. Kim, W.-W., Menon, S.: A new incompressible solver for large-eddy simulations. Int. J. Numer. Methods Fluids **31**, 983 (1999)
35. Driscoll, R.J., Kennedy, L.A.: A model for the turbulent energy spectrum. Phys. Fluids **26**, 1228 (1983)
36. Wei, T., Willmarth, W.W.: Reynolds number effects on the structure of a turbulent channel flow. J. Fluid Mech. **204**, 57 (1989)
37. Nikitin, N.V., Nicoud, F., Wasistho, B., Squires, K.D., Spalart, P.R.: An approach to wall modeling in large eddy simulations. Phys. Fluids **12**, 1629 (2000)
38. Fureby, C., Alin, N., Wikström, N., Menon, S., Persson, L., Svanstedt, N.: On large eddy simulations of high Re-number wall bounded flows. AIAA J. **42**, 457–468 (2004)
39. Grinstein, F.F., Oran, E.S., Boris, J.P.: Pressure field, feedback and global instabilities of subsonic spatially developing mixing layers. Phys. Fluids **3**(10), 2401–2409 (1991)
40. Grinstein, F.F., DeVore, C.R.: On global instabilities in countercurrent jets. Phys. Fluids **14**(3), 1095–1100 (2002)

41. Grinstein, F.F.: Vortex dynamics and entrainment in regular free jets. J. Fluid Mech. **437**, 69–101 (2001)
42. Grinstein, F.F.: On integrating large eddy simulation and laboratory turbulent flow experiments. Philos. Trans. R. Soc. Lond. A **367**(1899), 2931–2945 (2009)
43. Hussain, F., Husain, H.S.: Elliptic jets. Part I. Characteristics of unexcited and excited jets. J. Fluid Mech. **208**, 257–320 (1989)
44. Wetzel, T.G., Simpson, R.L., Chesnakas, C.J.: Measurement of three-dimensional crossflow separation. AIAA J. **36**, 557–564 (1998)
45. Alin, N., Svennberg, U., Fureby, C.: Large eddy simulation of flows past simplified submarine hulls. In: Proc. 8th Int'l Conf. Numerical Ship Hydrodynamics, Busan, Korea, pp. 208–222 (2003)
46. Groves, N.C., Huang, T.T., Chang, M.S.: Geometric characteristics of DARPA SUBOFF models. Report DTRC/SHD-1298-01, David Taylor Research Ctr. (1989)
47. Huang, T.T., et al.: Measurements of flows over an axisymmetric body with various appendages (DARPA SUBOFF experiments). In: Proc. 19th Symp. Naval Hydrodynamics, Seoul, Korea (1992)